

Visual hull based 3D reconstruction of shocks in under-expanded supersonic bevelled jets

Lim, Desmond Haoxiang; New, Tze How; Mariani, Raffaello; Cui, Y. D.

2018

Lim, D. H., New, T. H., Mariani, R., & Cui, Y. D. (2018). Visual hull based 3D reconstruction of shocks in under-expanded supersonic bevelled jets. *Experimental Thermal and Fluid Science*, 99, 458-473. doi:10.1016/j.expthermflusci.2018.08.022

<https://hdl.handle.net/10356/107562>

<https://doi.org/10.1016/j.expthermflusci.2018.08.022>

© 2018 Elsevier Inc. All rights reserved. This paper was published in *Experimental Thermal and Fluid Science* and is made available with permission of Elsevier Inc.

Downloaded on 13 Mar 2024 15:17:45 SGT

Visual-hull based 3D reconstruction of shocks in under-expanded supersonic bevelled jets

H. D. Lim¹, T. H. New^{1,*}, R. Mariani¹ and Y. D. Cui²

¹School of Mechanical and Aerospace Engineering, Nanyang Technological University, 50 Nanyang Avenue, Singapore 639798, Republic of Singapore

²Temasek Laboratories, National University of Singapore, 5A Engineering Drive 1, Singapore 117411, Republic of Singapore

Abstract

Three-dimensional shock structures produced by Mach 1.45 supersonic bevelled jets were digitally reconstructed based on schlieren photography and a voxel-based visual hull technique. By taking advantage of the strong edge features commonly found in schlieren images of shock waves, the proposed technique demonstrates the possibility of performing shock wave reconstruction in supersonic jet applications without prior knowledge of the global density or velocity field. Semi-synthetic camera parameters were introduced as a method to circumvent camera calibration issues faced in the reconstruction procedure. This is key to achieving accurate and high-resolution reconstructed shock waves for both axisymmetric and asymmetric test cases with an average of 2.5% error when validated against raw schlieren images. When applied to bevelled jets with non-uniform nozzle exit geometries, an additional assumption was made to address the problem of schlieren line-of-sight blockage by the non-conventional nozzle, and reconstruction errors were found to be larger near regions of poorer shock wave contrast. Current results indicate that the technique is robust and fast during image calibration and processing, with accuracy of reconstructed shock waves in both conventional and non-conventional nozzles strongly dependent on shock wave contrast. Compared to existing techniques that can be used to reconstruct 3D shock structures, the proposed technique has the advantage of being totally non-intrusive as compared to point or particle-based measurements, requires significantly less computation

Lim H.D., New T.H., Mariani R. and Cui Y.D. (2018) Visual-hull based 3D reconstruction of shocks in under-expanded supersonic bevelled jets. Experimental Thermal and Fluid Science, Vol. 99, pp. 458-473

than tomographic methods, offers high resolution reconstruction even with limited camera resolution and projected schlieren views, and is easy and cost effective to implement.

Keywords: Schlieren; three-dimensional image processing; flow diagnostics; camera calibration; visual hull; supersonic jets

*Corresponding author: dthnew@ntu.edu.sg

1. Introduction

The potential core and shock structures associated with free under-expanded supersonic jets have drawn considerable attention in supersonic flow studies. Nevertheless, only the Mach disk location shows good agreement across different studies such that it can be accurately predicted by empirical relations [1]. Parameters such as the intercepting shock diameter or length of first shock cell have limited amount of experimental or validated numerical simulation data available for any conclusive and unifying relation to be drawn, with some existing results showing large discrepancies of up to 100% [1]. Much of the supersonic jet literature has also been conducted on axisymmetric nozzles [2-10], with lesser attention paid to modified nozzle exit geometries. While changing the nozzle exit geometry has been shown to be an effective passive flow control technique in both subsonic [11-13] and supersonic jets [14-16], there is limited amount of experimental data available to validate numerical simulations. This can be attributed to difficulties in conducting experiments on supersonic jets to accurately map 3D shock structures. Most current approaches are difficult to implement, computationally demanding and/or require expensive equipment, and these challenges need to be overcome before extensive optimization studies on supersonic jet nozzle designs can be conducted.

Current methods that offer insights to shock structures include point measurement techniques such as hot wire anemometry and pressure probes, particle-based techniques such as two-dimensional (2D) particle image velocimetry (PIV) and tomographic PIV, and non-intrusive techniques such as schlieren and tomographic Background-Oriented Schlieren (BOS). Hot wire anemometry and pressure probes are ill-suited for supersonic jet measurements as they are inherently intrusive by nature, leading to issues such as mechanical vibrations and the formation of unwanted shocks due to their disturbance in the flow field. The use of point

measurement techniques to obtain 3D shock structures is also very inefficient due to the large number of required sampling points.

Seeding-based techniques such as 2D cross-correlation PIV or tomographic PIV are less intrusive and allow 3D shock structures to be inferred from global velocity field data. However, particle-based approaches are based on the assumption that seeding particles can faithfully track air particles in compressible flows and turbulent flow structures, including across complex shock waves whereby there are sharp changes in flow properties. In reality, seeding particle distributions are often non-uniform in such flow scenarios, which can be further complicated by particle agglomeration effects. While the use of sub-micron seeding particles can reduce seeding particle drag and alleviate particle tracking uncertainties, high-power light sources would have to be employed to compensate for the loss of light scattering efficiency in smaller particles. This may be an impractical option due to economical or safety reasons. Resolution of the resulting velocity fields may also be limited by the cross-correlation window matching approach in post-processing, which could lead to failures in resolving the smaller-scale flow structures. Image blurring may also occur due to significant refractive index gradients across shocks.

In the case of tomographic PIV, the challenge of controlling the seeding density is even more severe as a delicate balance must be maintained between having sufficiently large number of particles for 3D cross-correlation to be performed and having low number of particles to reduce the presence of ghost particle artefacts. Storage and processing of data are also highly challenging as large amount of information is required in order to conduct temporal averaging and accurately resolve shock positions. Because of the severe challenges listed above, there has only been one successful application of tomographic PIV in a heated Mach

1.4 under-expanded supersonic jet flow, with full 3D reconstruction of the Mach disk and barrel shocks achieved [4].

Schlieren-based techniques are generally favoured for shock wave visualization purposes as they are totally non-intrusive, of relative ease in experimental design, and suitable for visualizing flows with strong density variations. Traditionally, schlieren and shadowgraph techniques have been employed for 2D visualization of flow phenomena in inhomogeneous mediums. In the past two decades, the advent of digital cameras and image-processing techniques have brought about significant developments and notable strides [17] in quantitative schlieren techniques such as BOS [18-20] and schlieren velocimetry [21]. Despite the popularity of schlieren techniques for shock visualizations, and the inherent three-dimensionality of most real-world shocks, there have been limited attempts at digitally reconstructing 3D shock structures.

Among the schlieren-based techniques, tomographic BOS has the capability of recovering the 3D density field of a flow phenomenon, thus allowing shock structures to be inferred or digitally reconstructed. This technique typically involves the use of optical flow or cross-correlation approaches to obtain displacement vectors of density gradients, obtaining the light-path integrated density field by solution of the Poisson equation, and using filtered back-projection techniques to obtain the final 3D density field. Similar to tomographic PIV whereby the global 3D velocity field is required before shock waves can be reconstructed, tomographic BOS technique requires the global 3D density field to be known before the reconstruction of shock waves is possible. Current relevant applications of tomographic BOS include obtaining 3D shock structures from supersonic flow over cones [22, 23] and under-expanded axisymmetric jets [5], the reconstruction of unsteady and asymmetric hot gas

flow's density field using a synchronized 16 cameras configuration [24], and the reconstruction of low speed plume flows using a 12 cameras configuration by posing the problem in an optimization framework [25]. However, the tomographic BOS technique has its own challenges which include image blurring across shocks with significant refractive index change, calibration issues when dealing with multiple camera configurations [26], large memory requirements and computational cost (including during the camera calibration stage), as well as limited resolution of shock waves when computed density fields are reconstructed from a limited number of camera views or with low resolution cameras.

The novel voxel-based visual hull technique described in the manuscript is capable of circumventing the challenges commonly faced by the techniques currently available to researchers. By taking advantage of the strong edge features commonly observed in schlieren images of shock waves, direct reconstruction using voxel-based visual hull (VH) technique is possible without first needing to derive an additional field quantity, such as velocity in velocimetry-based techniques or density in quantitative schlieren techniques. This approach offers several key advantages over current 3D techniques, including reductions in computational time, low hardware requirement during post-processing, inexpensive experimental setup, ease of implementation, as well as the ability to achieve high resolution and accurate reconstructed shocks even when using limited number of camera views or with low resolution cameras. Not only does it extend the functionality of existing schlieren systems available in most compressible flow research laboratories to achieve quantifiable shock structure characteristics, it can also be used for challenging hypersonic flows or to provide experimental data to validate steady-state simulations (where unsteady viscous effects are not captured).

The present study on moderately under-expanded bevelled jets produced stable shock structures which allow images at different view angles to be captured at different time instances. Coupled with the use of an in-house developed semi-synthetic camera calibration technique, multiple camera calibration issues commonly faced by tomographic techniques in asymmetric test cases can be avoided while simultaneously providing very precise camera parameters in the current miniature reconstruction application. The application of voxel-based VH technique for reconstructing shock structures based on schlieren photography has demonstrated the potential of providing accurate quantitative geometrical information to further complement shock structure visualizations. As such, the technique developed here provides an alternative experimental technique that is well-suited for optimization studies, contributes towards improving the understanding of shock systems from an experimental point of view, as well as bridging the gap between numerical simulations and experimental work by providing accurate data to validate the former.

2. Reconstruction techniques

Three-dimensional reconstructions from multiple 2D images may be broadly classified into structure-from-motion [27, 28] and shape-from-silhouette techniques [29, 30]. In structure-from-motion techniques, reconstruction of a static scene is achieved by moving a single camera to multiple positions and capturing images from different viewpoints. This is also equivalent to the multi-view stereo technique whereby multiple synchronized cameras at different viewpoints capture an image of a static scene simultaneously. Full knowledge of the camera parameters is required, necessitating a camera calibration involving an external calibration board. Once the camera calibration is completed and the stereo images captured, the correspondence problem must be solved before 3D recovery of a structure using triangulation and surface fitting methods is possible. This is traditionally the most difficult

problem for stereo analysis approaches, and common techniques to deal with the correspondence problem include template matching or feature matching schemes. Popular related methods include direct cross-correlation, Scale Invariant Feature Transform (SIFT) [31] and Speeded Up Robust Features (SURF) [32]. It must be emphasized that multi-view stereo techniques are only capable of reconstructing stereoscopic scenes which provide depth perception to the viewer, and do not offer full 3D information regardless of the viewing angle. More importantly, it is very challenging to apply stereo reconstruction techniques on schlieren images of shock waves due to the integrative nature of schlieren and the lack of features or textures on the surface of shock structures.

On the other hand, shape-from-silhouette techniques rely on the construction of volumes or surfaces in the scene such that the reconstruction is consistent with the input silhouette images from different viewpoints. This idea was first introduced by Baumgart [33], and shapes reconstructed from this approach were subsequently termed “visual hull” (VH) by Laurentini [34]. More concisely, VH was defined as an object’s maximal geometrical representation that is consistent with silhouette images from any viewpoints lying outside the object’s convex hull. The VH approach for 3D reconstruction has several key advantages. Firstly, the reconstructed object is fully 3D and thus allows a more complete visualization of the reconstructed object and has the potential of extracting important geometrical information. Secondly, VH implementation is relatively straightforward from the perspectives of both experimental setup and data processing, especially when compared to multi-view stereo techniques which require special attention for the correspondence problem to be solved [31, 32]. Thirdly, silhouette-based approaches are good fits with schlieren techniques, whereby “shadow”-like intensity patterns are created due to density variations

along the optical light path. Finally, as opposed to multi-view stereo methods, VH methods are inherently more robust, and allow the

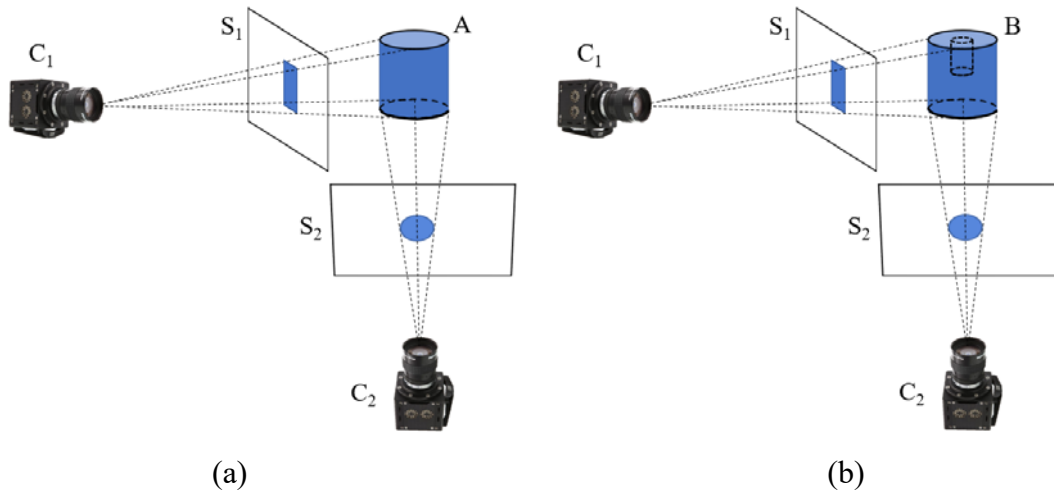


Fig. 1 Illustration of the voxel-based VH technique with (a) convex object (b) concave object

integration of a semi-synthetic camera calibration technique which serves to relax the requirements on experimental camera calibration, while providing reasonably accurate reconstruction of miniature objects typically encountered during scaled-down testing.

Despite the advantages and attractiveness of the VH approach, there are some limitations which restrict its application in reconstruction problems. Under the assumption that no viewpoints lie inside an object's convex hull, the VH approach performs poorly when reconstructing concave objects due to the inability of the visual cone in resolving concavities. This is best elucidated in Fig. 1, where two cameras capturing images of a convex object (a solid cylinder) is illustrated in Fig. 1(a), while Fig. 1(b) depicts the exact same setup but with a concave object (cylinder with a hole in the centre). Here, it should be highlighted that the convex hull of object B in Fig. 1(b) has the exact same geometry as Fig 1(a)'s object A. Object A can be reconstructed with sufficient accuracy if there is a sufficient number of cameras positioned at different viewing angles. However, object B can never be accurately reconstructed even with an infinite number of cameras, due to the assumption of no

viewpoints lying inside B's convex hull, which leads to a lack of information on the concavity. VH reconstruction also requires multiple viewpoints to achieve accurate results, and this is usually not feasible in dynamic scenes which restricts VH applications to static scenes.

Two main categories of VH techniques have the capabilities of achieving full 3D reconstruction of an object: surface-based [35], and voxel-based [34] VH technique. Surface-based VH technique uses polyhedral surfaces to represent the VH, which is constructed using points, edges and faces generated through the intersection of occluding contours projected from silhouette images. It is computationally less intensive than the voxel-based VH method, and can avoid space discretization problems which may result in visually boxy VH. However, numerical instability is an issue when dealing with complex objects, and implementation is not as straightforward as the voxel-based VH technique. The voxel-based VH approach is preferred for the current application as there is no requirement for real-time reconstruction, and numerical stability is also guaranteed which allows the technique to be potentially extended to more complex flow scenarios. The voxel-based VH technique relies on a systematic volume carving approach to arrive at a volumetric representation of the object's VH.

As illustrated in Fig. 2(a), a pre-defined tessellation of cubic voxels is sampled and subjected to a binary decision-making process when visual cones ($VC_{i=1,2,...n}$) are projected from the camera centre ($C_{i=1,2,...n}$) and silhouette images ($S_{i=1,2,...n}$) into the tessellation. Sampled voxels that do not belong in the projected visual cone are discarded, while the remaining voxels constitute the object's approximate VH. Figure 2(b) illustrates the difference between the original object and the approximate VH generated from two viewpoints. It can be inferred

that with an infinite image resolution and number of viewpoints, the approximate VH will become the object's true VH. In the rest of this manuscript, for the sake of brevity, the term "VH" will be used even if the number of viewpoints and the resolution of the silhouette images is finite.

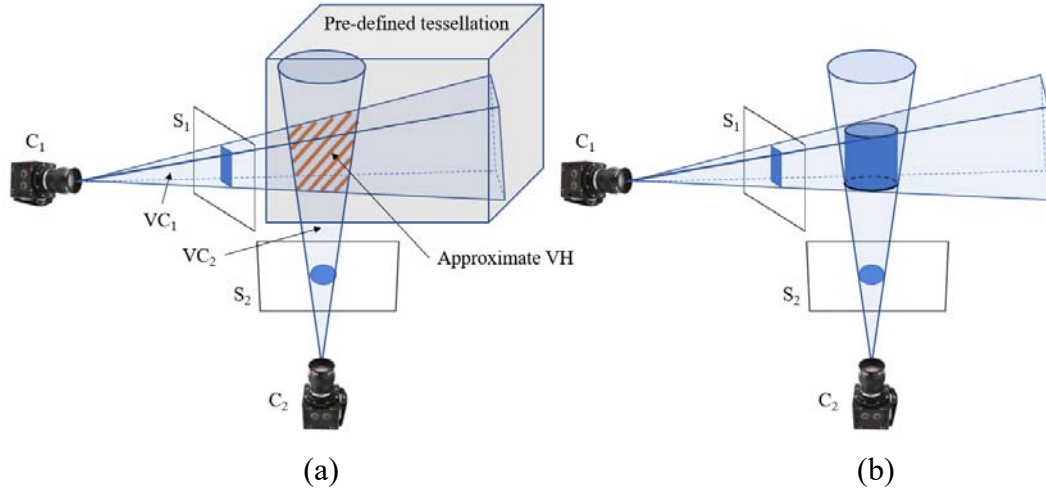


Fig. 2 Illustration of the volume carving concept (a) visual cones projected into the pre-defined tessellation (b) comparison with original object

3. Experimental methodology

In the previous section, limitations of voxel-based VH technique were highlighted. To circumvent the aforementioned limitations in this study, the following two assumptions were made. (#1) For the current shock reconstruction problem, shock systems to be reconstructed do not have any hidden features in geometrical concavities when the cameras are positioned orthogonal to the jet streamwise direction; (#2) shock systems are steady, and the use of a single camera capturing images at n number of viewpoints during different time instances offers the same results as using n number of cameras capturing images simultaneously. The first assumption was found to be reasonable from preliminary inspections of the captured schlieren images, whereby shock waves that are to be reconstructed were observed to be geometrically convex and relatively steady. The observations are also consistent with previous supersonic jet studies conducted at the same flow conditions [15]. The second

assumption was verified by capturing schlieren images at 1000FPS and observing no change in the positions of the shocks.

In order to obtain the reconstructed shock wave, two pieces of information are required. The first piece of information is the camera matrix C_n , which fully describes the spatial orientation and position of n number of cameras, as well as the focal length, optical centre and pixel skewness (if any) of the image. More information will be provided on the camera matrix in section 3.1. Ideally, the number of cameras at different viewing angles should be as large as possible as described in the previous section but is limited to 36 in the current application due to practicality. The choice of 36 was deemed to be sufficient based on the final resolution and accuracy of the reconstructed shock waves. Hence, 36 camera matrices are required in order to project the visual cones from its corresponding silhouette images.

The second piece of information is the silhouette or binary images describing the shock waves. The image intensity can be written as:

$$I_i(x, y) = \begin{cases} 1, & \text{for pixels lying within shock wave} \\ 0, & \text{for pixels lying outside shock wave} \end{cases} \quad (1)$$

where x and y represents the location of pixels in the image, and the subscript i represents the index of the image captured at a viewing angle. Keeping in mind of assumption (#2) which was made earlier, a single camera will be used to capture all 36 schlieren images at different viewing angles at different time instances. With the two pieces of information, standard volume carving can then be carried out to obtain the reconstructed shock wave.

The experimental methodology will be dissected into three sub-sections. Section 3.1 will focus on the external camera calibration and numerical procedures involved in generating the semi-synthetic camera parameters. Section 3.2 will focus on the experimental setup designed

to capture optimal schlieren images, and the numerical procedures undertaken to post-process the schlieren images into silhouette images. Section 3.3 will provide more information on the final volume carving step to generate the visual hull output. A flowchart that summarises chapter 3 is also provided in Fig. 3 to facilitate the discussion.

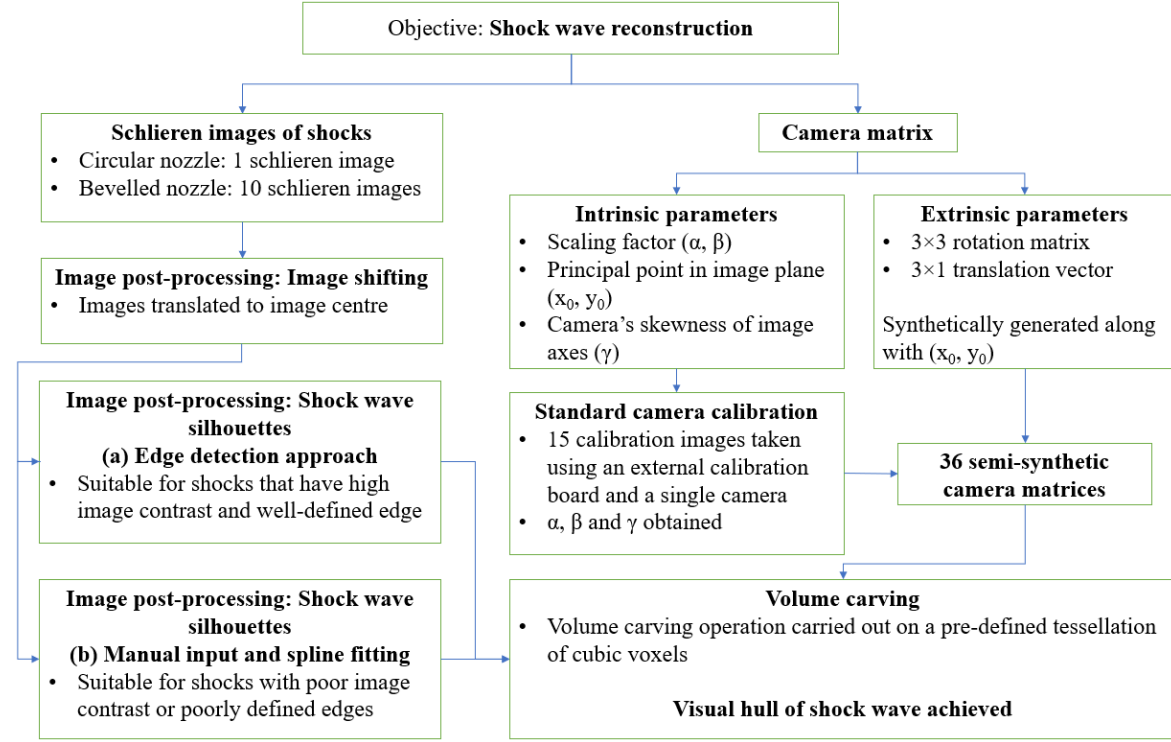


Fig. 3 Flowchart of experimental methodology

3.1 Semi-synthetic camera matrices

A pinhole camera model was used to provide a perspective transformation to relate world coordinates to image coordinates. This is illustrated in Eq. 2, whereby the camera matrix may be sub-divided into intrinsic and extrinsic parameters:

$$s \begin{bmatrix} x \\ y \\ 1 \end{bmatrix} = \underbrace{\begin{bmatrix} \alpha & \gamma & x_0 \\ 0 & \beta & y_0 \\ 0 & 0 & 1 \end{bmatrix}}_{\text{Intrinsic parameters}} \underbrace{\begin{bmatrix} r_{11} & r_{12} & r_{13} & t_1 \\ r_{21} & r_{22} & r_{23} & t_2 \\ r_{31} & r_{32} & r_{33} & t_3 \end{bmatrix}}_{\text{Extrinsic parameters}} \underbrace{\begin{bmatrix} X \\ Y \\ Z \\ 1 \end{bmatrix}}_{\text{World coordinates}} \quad (2)$$

s $\begin{bmatrix} x \\ y \\ 1 \end{bmatrix}$ $\begin{bmatrix} \alpha & \gamma & x_0 \\ 0 & \beta & y_0 \\ 0 & 0 & 1 \end{bmatrix}$ $\begin{bmatrix} r_{11} & r_{12} & r_{13} & t_1 \\ r_{21} & r_{22} & r_{23} & t_2 \\ r_{31} & r_{32} & r_{33} & t_3 \end{bmatrix}$ $\begin{bmatrix} X \\ Y \\ Z \\ 1 \end{bmatrix}$
 Image coordinates Intrinsic parameters Extrinsic parameters World coordinates

The intrinsic parameters describe the geometrical properties of a camera, with skewness of image axes represented by (γ) and is often assumed to be zero. The principal point or image

axes in the image plane is represented by (x_0, y_0) and is usually at the image centre. The focal length expressed in pixel units for image coordinates (x, y) is represented by (α, β) , and should have the same value theoretically. In practice, they may differ due to reasons such as camera lens distortion, camera calibration errors or anamorphic format image compression. The extrinsic parameters define the position and orientation of the real world relative to the camera, with the orientation described by the 3×3 rotation matrix and the position described by the 3×1 translation vector. Essentially, the camera matrix serves as a mapping function to relate 3D world coordinates to the 2D image coordinates. To obtain the solutions to the intrinsic and extrinsic camera parameters, an external calibration pattern with known dimensions is typically used along with standard nonlinear least-squares minimization Levenberg–Marquardt algorithm [36].

However, the use of the traditional camera calibration technique is not suitable for the current application. This was first discovered during initial testing, when a 0.9mm diameter Mach disk was generated by operating the jet at over-expanded condition at NPR 2.8, but failed to be accurately reconstructed. The extrinsic parameters were found to be lacking in accuracy, in part due to the miniature size of the reconstructed VH relative to the large projection distance of the camera to the VH, in part due to practical limitations during the camera calibration process. In this study, the diameter of the Mach disk was less than 1mm, while the projection distance was over 700mm. Hence, minute angular misalignments in the camera's orientation or position introduced by errors in the extrinsic parameters were able to contribute significantly to the final reconstructed VH. The use of a very small calibration pattern intended to maximise schlieren image resolution further exacerbated the problem of insufficient accuracy in the extrinsic parameters.

To obtain highly accurate camera parameters suitable for the current application, the intrinsic parameters γ , α and β were obtained using standard external camera calibration techniques while all other remaining camera parameters were synthetically generated. The synthetic extrinsic parameters were artificially generated to ensure perfect geometrical alignment of the cameras relative to the jet test section, hence overcoming the challenges faced during the initial testing. Additionally, there is also a need to control the principal point (x_0, y_0) although it belongs to the intrinsic parameters. This will be further discussed in section 3.2.2 due to its relationship with the image processing procedures. Since the intrinsic parameters are a property of the camera and lens, the same intrinsic parameters can be used throughout all 36 camera matrices.

With the use of synthetically generated extrinsic parameters, this means the cameras have shifted from their original positions and orientations, and there are certain implications on the captured images that one must be cautious with. In real world photography, light-carrying information of a 3D scene enters a camera and is recorded on a charge-coupled device (CCD) as a 2D image. A shift in the camera position or orientation will inevitably lead to a change in field-of-view, as well as changes in scene details such as object occlusion, object shadowing, reflectance, etc. Effectively, this leads to a very different set of information that can be recorded by the shifted camera. Images will require more than simple transformations in the form of scaling, rotation, or translation in order to correct them such that they can correspond to the new position and orientation of the shifted camera. However, the additional information to make the necessary correction is not available, as the original 2D image does not have the capability to fully capture information of a 3D scene.

Fortunately, it turns out that this constraint is not applicable in the context of schlieren imagery. In a schlieren setup, light rays are projected from a mirror or lens into the camera, and the information recorded by the CCD is an integration of the density variations along the entire light path. Assuming there are only slight changes in the camera position and orientation such that the schlieren light rays will still be able to project into the camera's CCD, the information recorded by the camera will not change since it is dependent only on the amount of refraction the light rays undergo. Hence, this relaxes the relationship between the extrinsic parameters and captured images, thus permitting the use of synthetically generated extrinsic parameters in the current application. It should be highlighted that while this approach takes advantage of the observation that the shock wave information in the schlieren images are invariant to slight changes in camera orientation and position, the exact location where the image forms on the CCD will still be affected by the change in extrinsic parameters. Hence, there remains a need to carry out image processing in terms of image translation, and adjustment of the principal point in the intrinsic parameters.

3.1.1 Traditional external camera calibration procedure

The intrinsic parameters γ , α and β were obtained by implementing external camera calibration technique using MATLAB's camera calibrator and a bespoke external calibration board, where the latter consisted of a 7×10 checkerboard pattern with 2.14mm squares prepared at a resolution of 1200 dpi. This board was positioned at the nozzle exit where the strongest shock waves were produced. A reference rotational angle of 0° was defined such that the board was squarely facing the camera, with the rotational axis of the board aligned with the jet axis. The alignment was ensured with the help of a self-levelling laser device. The board was rotated from -70° to 70° at regular intervals of 10° , hence capturing 15 calibration images. The precise rotation was achieved by mounting the calibration board on

an optomechanical instrument (Thorlabs RP01), which has graduation marks at 2° increment. The captured images were then post-processed to obtain the initial camera parameters, with an overall mean error of 0.63 pixels. The intrinsic parameters were retained while the extrinsic parameters were discarded.

It should be highlighted that since the purpose of the external calibration conducted here is to obtain only the intrinsic parameters, the described procedure regarding the alignment and precise rotation of the calibration board does not have to be strictly adhered to. However, closely following the procedures as described above instead of choosing random angles to position the calibration board were found to be optimal in ensuring alignment of the board's rotational axis with the jet axis across all 15 calibration images, thus ensuring that the focal lengths (α , β) obtained are as accurate and consistent as possible.

In theory, keeping the camera stationary while rotating the calibration board at regular intervals of 10° (camera-centric view) is equivalent to keeping the calibration board stationary and moving the camera at 10° interval around the azimuthal position of the jet (pattern-centric view). For the case of the initial testing first mentioned in section 3.1 whereby attempts to recover the Mach disk was unsuccessful, the full camera matrices (both intrinsic and extrinsic parameters) were required to be obtained purely from external camera calibration. Hence, the procedures as described above must be strictly followed to obtain camera matrices that are as accurate as possible.

3.1.2 Generating synthetic extrinsic parameters

The locations and orientations of the 36 cameras that were synthetically generated is illustrated in Fig. 4, with Fig. 4(a) illustrating cameras in the first quadrant pointing towards

the jet axis. Figure 4(b) illustrates all 36 cameras lying on the perimeter of a perfect circle in a 2D YZ-plane, with the radius of the circle representing the focal length of the camera in world coordinates. The focal length f can be obtained by:

$$f = \frac{\alpha + \beta}{2} \times M \quad (3)$$

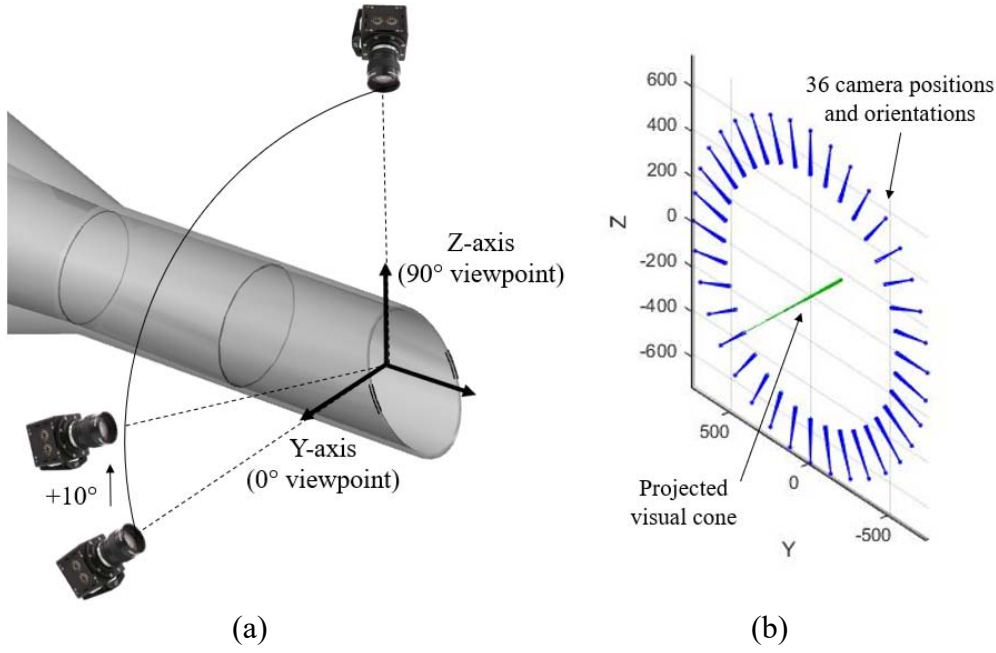


Fig. 4 Positions and orientations of the cameras generated with synthetic extrinsic parameters (a) cameras pointing towards bevelled jet axis (b) cameras forming a circle on YZ-plane

where M represents the pixel-to-world magnification factor obtained from the calibration board. The rotational matrix R and translation vector T were synthetically generated with the following equations:

$$R_i = \begin{bmatrix} 1 & 0 & 0 \\ 0 & \cos(\theta_{x,i}) & -\sin(\theta_{x,i}) \\ 0 & \sin(\theta_{x,i}) & \cos(\theta_{x,i}) \end{bmatrix} \quad (4)$$

$$T_i = -R_i \times C_i \quad (5)$$

where $\theta_{x,i}$ represents the azimuthal rotational angle and C_i represents the column vector containing the camera position in world coordinates (X, Y, Z). The first camera position was

defined at $C_1 = (0, f, 0)$, with $\theta_{x,1} = \frac{\pi}{2}$. Subsequent camera positions and orientations were then obtained by numerically rotating the first camera about the streamwise direction, or vector $(1, 0, 0)$, by 10° incrementally. Mathematically, this is the same as performing a rotation of a 3D point about the X-axis. In equation form, this can be written as:

$$\theta_{x,i+1} = \theta_{x,i} + 10^\circ \times \frac{\pi}{180^\circ} \quad (6)$$

$$C_{i+1} = \begin{bmatrix} 1 & 0 & 0 \\ 0 & 0.9848 & 0.1736 \\ 0 & -0.1736 & 0.9848 \end{bmatrix} \times C_i \quad (7)$$

where the matrix in Eq. 7 can be obtained by taking the transpose of Eq. 4 and using 10° rotation angle. Thirty-six cameras with precisely known positions and orientations can then be generated, as illustrated in Fig. 4(b).

3.2 Generation of silhouette images

3.2.1 Schlieren images

Schlieren experiments were conducted using a modified double-mirror Z-type system for supersonic jets with a design Mach number of 1.45 for a nozzle pressure ratio (NPR) of 3.4 [15]. A 200W light emitting diode (LED) provided broadband illumination during the experiments. An aperture served to improve the spatial coherence of the light source. Two $f/10$, 3m focal length, 300mm diameter parabolic surface mirrors reflected light into the test section and onto a vertical knife-edge at the tangential focus. An IDT NX4-S1 camera with a Nikon AF Micro-Nikkor 200mm f/4D IF-ED lens was used to capture schlieren images at $1024\text{px} \times 1024\text{px}$ resolution and 1000FPS. The nozzle contraction ratio was 10.5, the nozzle exit inner diameter was 12.7mm and the nozzle exit lip thickness was 0.5mm. The experimental setup is shown in Fig. 5, with the modified double-mirror Z-type system preferred over the traditional double-mirror Z-type system due to advantages such as less laboratory space requirements, flexibility in optimizing the experimental setup to achieve

higher resolution images and allowing the high-speed camera to be focused on the jet axis during camera calibration. Experiments were conducted at under-expanded exhaust conditions at NPR 4.0 and 5.0 for the baseline circular and a 30° bevelled nozzle [15]. In this paper, all schlieren images presented are the raw image unless otherwise stated.

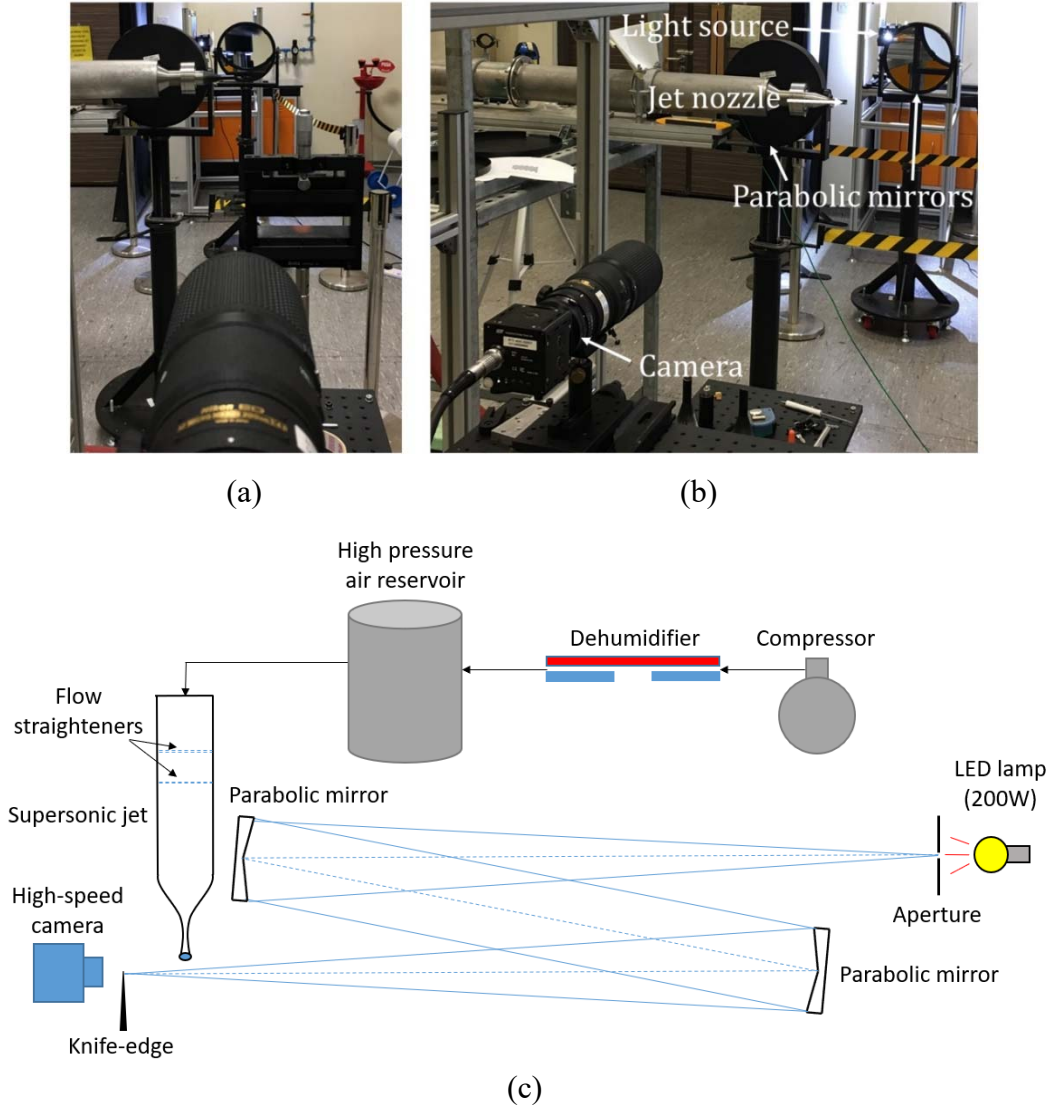


Fig. 5 Modified Z-type double-mirror schlieren setup (a) viewpoint 1 (b) viewpoint 2 (c) schematic diagram

In Fig. 6, contrast and brightness enhanced schlieren images of the circular jet at NPR 5.0 captured during initial testing are illustrated. Figures 6(a), 6(b) and 6(c) show the images captured using the horizontal knife-edge (HKE) placed at the sagittal focus, with exposure time increasing from 0.77 μ s to 30 μ s. Figures 6(d) and 6(e) shows the images captured using

the vertical knife-edge (VKE) placed at the tangential focus, with exposure time of $30\mu\text{s}$ and $494\mu\text{s}$ respectively. Figure 6(f) shows the picture of a shadowgraph taken with an exposure time of $12\mu\text{s}$. Optimal images for the current application were found to be taken by using a long exposure time of over $400\mu\text{s}$ along with a vertical knife-edge. The use of a longer exposure

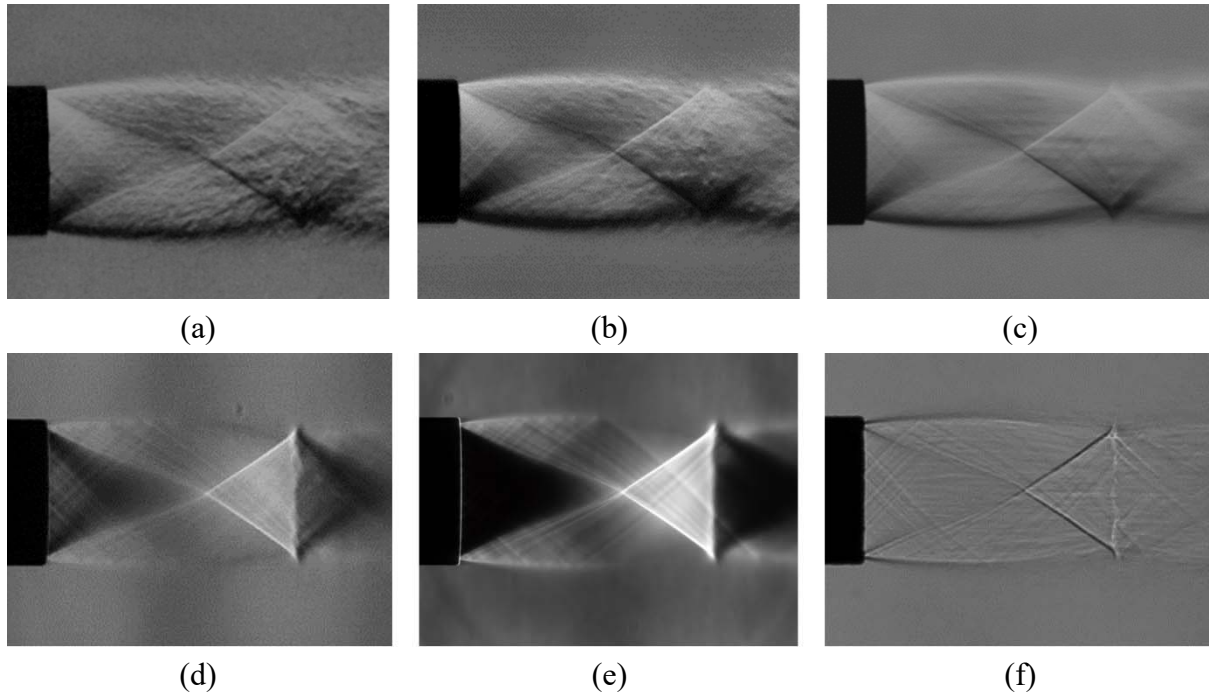


Fig. 6 Enhanced test images of the circular jet at NPR 5.0 (a) HKE schlieren, $0.77\mu\text{s}$ (b) HKE schlieren, $1\mu\text{s}$ (c) HKE schlieren, $30\mu\text{s}$ (d) VKE schlieren, $30\mu\text{s}$ (e) VKE schlieren, $494\mu\text{s}$ (f) shadowgraph, $12\mu\text{s}$

time was able to reduce the influence of turbulent structures, and it also allows a much greater cut-off at the knife-edge which creates over-ranging of the expansion and compression zones. This greatly improved the contrast of the intercepting and reflected shocks, while also reducing visibility of unwanted faint shocks that were otherwise visible in Figs. 6(d) and 6(f). In this study, all schlieren images were captured with an exposure time of over $400\mu\text{s}$, with the vertical knife-edge adjusted to about 80% cut-off.

For the reconstruction, 36 images captured at azimuthal angular interval of 10° are required in order to provide the silhouette images for the 36 semi-synthetic camera matrices. However, this was not necessary for the baseline nozzle where the shock systems were expected to be axisymmetric. The axisymmetric property of the baseline shock systems was verified by taking schlieren images of the shock structures from multiple different viewing angles during the study. Specific to the baseline nozzle, only a single image was taken from one viewpoint. Once

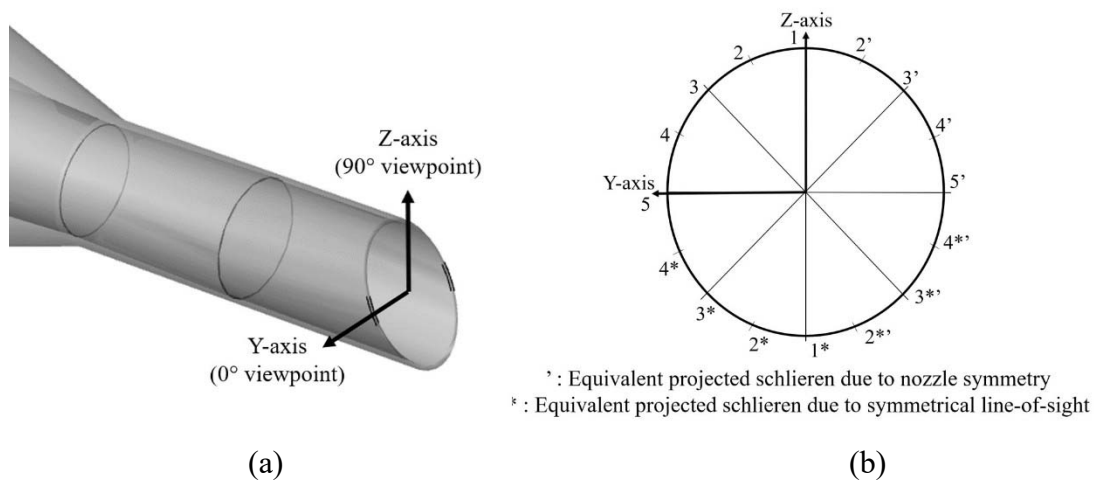


Fig. 7 (a) Bevelled nozzle drawing with azimuthal angle defined and (b) illustration of equivalent schlieren projection views

the image has been processed to generate the silhouette image, it will be duplicated and used as the silhouette images for all 36 viewpoints. For the bevelled nozzles, nozzle symmetry about the Z-axis and schlieren line-of-sight symmetry effectively limits the angles of unique schlieren's projected views to a single 90-degree quadrant. A schematic to illustrate this property is shown in Fig. 7. Hence, 10 schlieren images were captured at regular intervals of 10° , within the range of $[0, 90]$ degrees. This was achieved by rotating the nozzle with the help of a bespoke circular ruler fixed onto the circular bracket clamping the detachable nozzle in position. The error associated with the azimuthal rotational angle was estimated to be about 1° based on the bespoke circular ruler. With every nozzle rotation of 10° , the reflection point of the bevelled jet operated at NPR 5.0 shifted by about 4 pixels. Hence, a rotational

error of 1° translates to an image pixel error of 0.4 pixels which is negligible. The acquired schlieren images were post-processed into silhouette images, before being reflected about both symmetry axis to obtain 36 silhouette images in the range of $[0, 360]$ degrees.

3.2.2 Image post-processing procedures

With the use of synthetic extrinsic parameters, cameras are enforced to point straight at the jet axis. Consequently, this would mean that for the captured images, the image row in which the

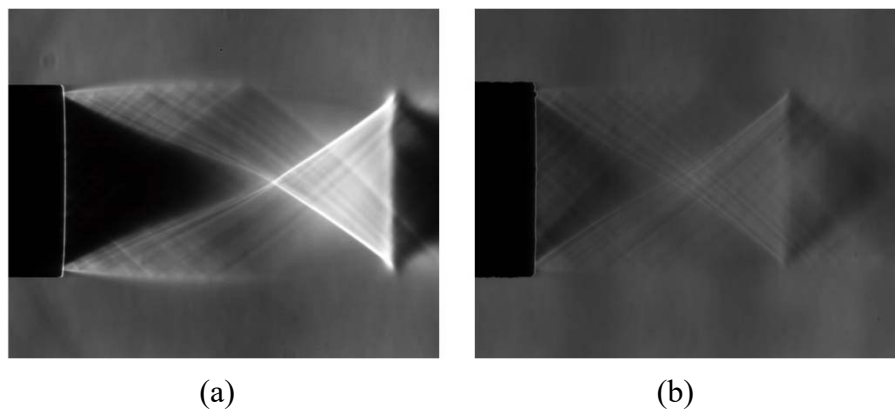


Fig. 8 Schlieren images of circular jet operated at (a) NPR 5.0 (b) NPR 4.0

jet axis can be located should be at the image centre. Furthermore, the tip of the nozzle should appear in the same image column across all captured images. Hence, all captured schlieren images were translated by using the nozzle outer diameter and the nozzle tip as reference, with zeroes padding the image borders. Because of the image translation, the principal point (x_0, y_0) of all 36 camera matrices was redefined at the image centre with pixel location of (512.5, 512.5).

Before the schlieren images can be used together with the camera matrices to perform reconstruction, they have to be processed into silhouette images first. The procedure to process the schlieren images into silhouette images is dependent on the characteristics of the schlieren images captured. In Fig. 8(a), the circular jet operated at NPR 5.0 shows good

contrast of shock waves' pixel intensity relative to the background, with well-defined shock wave edges. For such images, the silhouette images were generated using the edge detection method, which was found to be stable when applied to schlieren images with these characteristics. In Fig. 8(b), the circular jet operated at NPR 4.0 shows shock wave edges which are still sufficiently strong to enable detection by the edge detection method. However, the presence of weaker shocks with similar edge contrast throughout the entire flow region effectively decreases the signal to noise ratio (SNR). This leads to spurious edges being detected but cannot be filtered out efficiently,

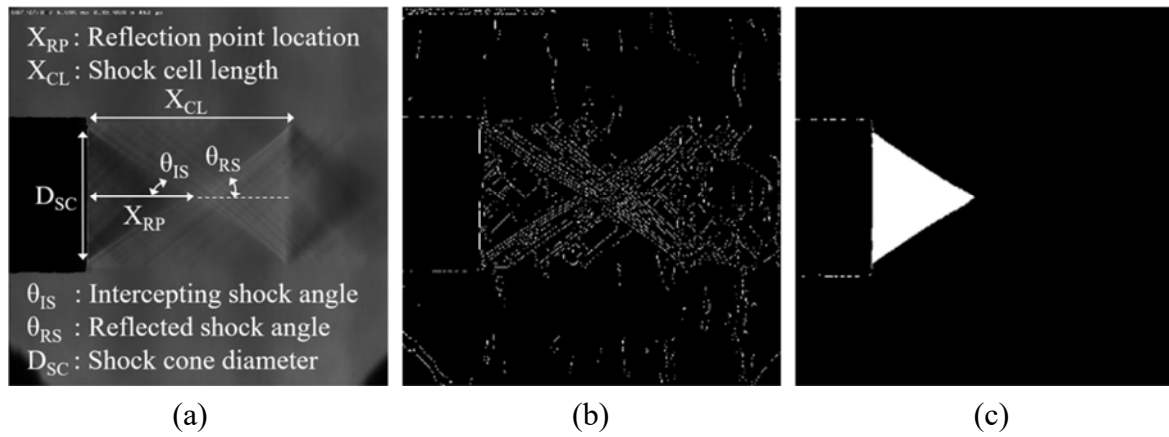


Fig. 9 Shock structures of an under-expanded baseline jet (NPR 4.0) (a) schlieren (b) noisy edge map (c) silhouette of shock wave

hence reducing the reliability of the edge detection method in such a scenario. For images where the edge detection fails, the algorithm switches to a manual spline fitting method. Both the edge detection method and the manual spline fitting method will be further discussed.

Edge detection method

In the edge detection approach, schlieren images were processed with MATLAB's edge detection using the canny method, which includes gaussian image smoothing as a pre-step to reduce the influence of image noise. The process converts schlieren images as illustrated in

Fig. 9(a) into obtain edge maps (or binary images), shown in Fig. 9(b). Unlike edge detection of the nozzle which was relatively straightforward due to the strong contrast between the nozzle outline and the schlieren background, the edge map which includes the shock wave edges were usually much noisier due to the use of a weaker edge detection threshold, and denoising was necessary before silhouette images (see Fig. 9(c)) can be generated. To achieve this, area opening operation which removes connected components that have lesser number of pixels than a specified threshold was performed. This essentially acts like a filter that can remove the low wavelength noise, with the resulting image consisting of the shock wave edges and a small number of high wavelength noise – long continuous edges scattered in the background. The

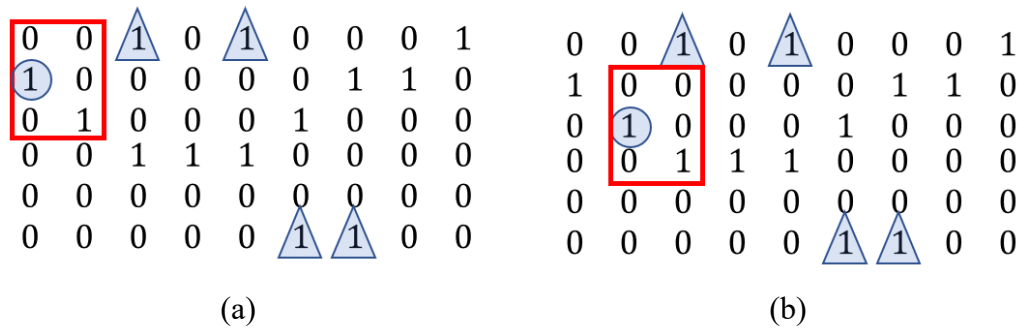


Fig. 10 Image intensity and the window search process at (a) current iteration (b) next iteration

remaining noisy edges were difficult to remove efficiently using filters due to their strong similarity with the shock wave edges, sensitivity to canny edge function's input parameters, and low robustness when handling schlieren images across different test cases.

To identify the pixel locations of the shock wave edges, a 2×7 pixels vertical window was initialized on the shock wave edge, and dynamically shifted to search neighbouring pixels for shock wave edges. Pixels of non-zero value that managed to enter the window during the search was accepted as part of the shock wave edge, with the new-found pixel location used in the next iteration to initialize the next window. The stoppage criterion was set at the first

occurrence of either 5000 iterations or arrival at the nozzle edges, which was pre-determined earlier. The vertical rectangular window was chosen to accommodate for shock waves with large angles. Removal of noise during the area opening operation and the choice of a relatively small window ensures noisy edges did not enter the window during the window search process. A simple illustration to describe this process is provided in Fig 10, whereby a 2×3 pixels vertical window is represented by the red rectangle, pixel intensity of 1 represents the shock wave edge, pixel intensity of 1 with the blue triangle represents unwanted image noise, and the blue circle represents the pixel location used to initialize the search window at the current iteration. In Fig. 10(a), a non-zero value pixel manages to enter the window at the bottom right corner and is thus labelled and recorded as part of the shock wave edge. This pixel then becomes the new location to initialize the search window at the next iteration, as illustrated by Fig. 10(b). The process repeats itself until the stoppage criteria is fulfilled.

Manual spline fitting method

In the manual spline fitting approach, approximately 5 to 9 points along the shock wave in the schlieren image were manually selected, thus allowing linear or Hermite's cubic interpolative splines approximating the shock waves to be fitted automatically. The linear splines were created by using the following parametric equations:

$$y_{interpolated}^{(m)} = y_m + (y_{m+1} - y_m) t \quad (8)$$

$$x_{interpolated}^{(m)} = x_m + (x_{m+1} - x_m) t \quad (9)$$

where t is the parametric parameter, (x_m, y_m) represents the coordinates of the m^{th} selected data point, and the superscript (m) represents the spline segment index. Following the same notation, the cubic splines were created with the following parametric equations:

$$y_{interpolated}^{(m)} = A_y^{(m)}t^3 + B_y^{(m)}t^2 + C_y^{(m)}t + D_y^{(m)} \quad (10)$$

$$x_{interpolated}^{(m)} = A_x^{(m)}t^3 + B_x^{(m)}t^2 + C_x^{(m)}t + D_x^{(m)} \quad (11)$$

For each cubic spline segment, the parameters $A_x^{(m)}$, $B_x^{(m)}$, $C_x^{(m)}$ and $D_x^{(m)}$ can be determined by using the Hermite matrix:

$$\begin{bmatrix} A_x^{(m)} \\ B_x^{(m)} \\ C_x^{(m)} \\ D_x^{(m)} \end{bmatrix} = \begin{bmatrix} 2 & -2 & 1 & 1 \\ -3 & 3 & -2 & -1 \\ 0 & 0 & 1 & 0 \\ 1 & 0 & 0 & 0 \end{bmatrix} \begin{bmatrix} x_m \\ x_{m+1} \\ x_m' \\ x_{m+1}' \end{bmatrix} \quad (12)$$

And the first order derivatives can be obtained by solving the following equation:

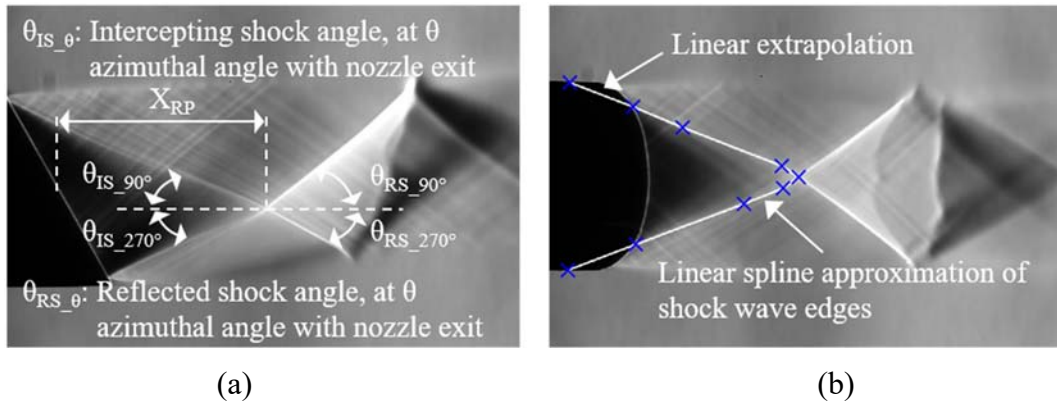


Fig. 11 Shock structures of an under-expanded bevelled jet (NPR 5.0) (a) schlieren at 0° viewpoint (b) schlieren at 90° viewpoint with linear spline approximating shock wave

$$\begin{bmatrix} 1 & 0 & 0 & 0 & \dots & 0 & 0 & 0 & 0 \\ 1 & 4 & 1 & 0 & \dots & 0 & 0 & 0 & 0 \\ 0 & 1 & 4 & 1 & \dots & 0 & 0 & 0 & 0 \\ 0 & 0 & 1 & 4 & \dots & 0 & 0 & 0 & 0 \\ \vdots & \vdots & \vdots & \vdots & \ddots & \vdots & \vdots & \vdots & \vdots \\ 0 & 0 & 0 & 0 & \dots & 4 & 1 & 0 & 0 \\ 0 & 0 & 0 & 0 & \dots & 1 & 4 & 1 & 0 \\ 0 & 0 & 0 & 0 & \dots & 0 & 1 & 4 & 1 \\ 0 & 0 & 0 & 0 & \dots & 0 & 0 & 0 & 1 \end{bmatrix} \begin{bmatrix} x'_0 \\ x'_1 \\ x'_2 \\ \vdots \\ x'_{N-1} \\ x'_N \end{bmatrix} = \begin{bmatrix} 1 \\ 3(x_2 - x_0) \\ 3(x_3 - x_1) \\ \vdots \\ 3(x_N - x_{N-2}) \\ 1 \end{bmatrix} \quad (13)$$

where N represents the total number of data points. The parameters A_y, B_y, C_y and D_y can be obtained with Eq. (12) and (13) using the same procedure, hence details are omitted for the sake of brevity.

The pixel locations of these fitted splines approximating the shock waves may then be extracted. An illustration of a linear spline fitted to approximate the intercepting shock edges from the bevelled nozzle is illustrated in Fig. 11(b). While the manual spline fitting method may appear primitive as compared to the fully automated edge detection method, it is unconditionally robust and still offers accurate reconstruction results. Both edge detection and manual spline fitting techniques were used interchangeably to process the schlieren images.

From Fig. 11(b), there is also an illustration of the shock wave edges being linearly extrapolated to the nozzle outer diameters. The bevelled nozzle incurred in the issue of information loss for shock waves lying upstream of the nozzle tip, due to schlieren line-of-sight blockage by the nozzle. To circumvent this problem and ensure the reconstructed shock cones are representative of the actual shock systems, local gradients were calculated, and this information was then used to linearly extrapolate the shocks towards the nozzle. With the shock wave edges identified through either the edge detection or the manual spline fitting method, the silhouette image as illustrated in Fig. 9(c) was then created by filling the pixels of the enclosed area bounded by the shock waves' edges with pixel value of one. The filling operation was conducted by performing a row-wise conversion of pixel value from zero to one, with the shock wave edges used to initialize the operation.

3.3 Volume carving

An initial bounding box with 30 million voxels was defined, and standard volume carving was carried out based on those parameters. Every single voxel in the initial bounding box was sampled and subjected to a binary decision, and voxels lying outside any of the 36 visual cones were rejected, with the remaining voxels constituting the visual hull that represents the shock structures. For reference, final voxels count typically ranged from 10% to 15% of the starting number of voxels, and the voxel sizes for the NPR 4.0 baseline jet are $0.044\text{mm} \times 0.044\text{mm} \times 0.044\text{mm}$. Since only the shock surfaces are of interest, they were extracted from the reconstructed VH and plotted with the CAD drawings of the nozzles. The extraction was achieved by sorting the VH's voxels into multiple XZ slices, and then searching each XZ slice for voxels with the maximum (minimum) x-coordinate value to obtain the shock surface of the intercepting shock (reflected shock). Here, it must be highlighted that the intercepting and reflected shocks were reconstructed separately, hence the search criterion would be able to yield the correct shock surfaces. The shock reconstruction algorithm was developed based on a standard volume carving visual hull code [37], and image processing was carried out on

a

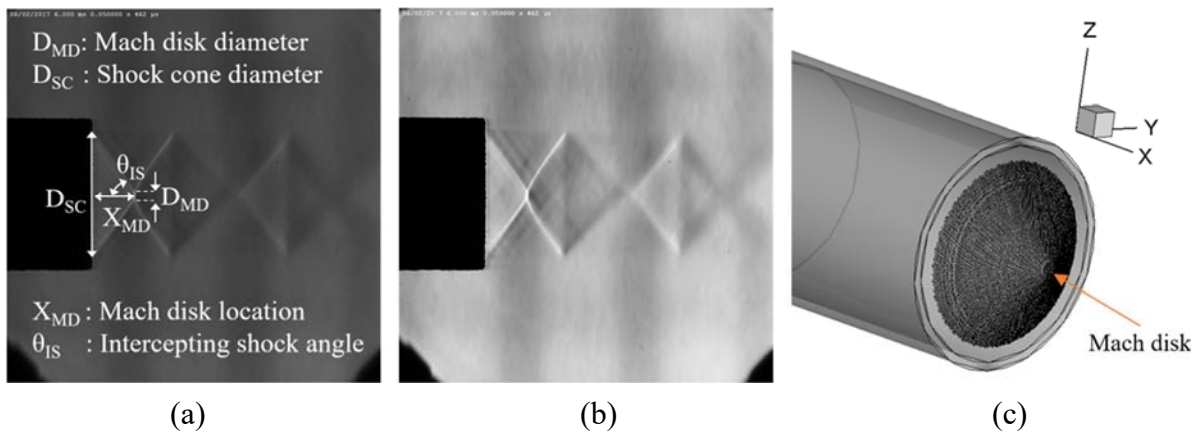


Fig. 12 Shock structures of an over-expanded baseline jet (NPR 2.8) (a) schlieren (b) contrast-enhanced schlieren (c) reconstructed results

Table 1: Reconstructed shock cone key parameters for baseline jet at NPR 2.8

	Schlieren images	Reconstructed shock cone
--	------------------	--------------------------

Baseline nozzle, over-expanded flow condition (NPR 2.8)		
D_{MD}	0.92 mm	0.90 mm
D_{SC}	11.25 mm	10.93 mm
X_{MD}	3.79 mm	3.77 mm
θ_{IS}	53.6°	53.1°

laptop with 8GB memory and an Intel® Core™ i7-5500U 2.4 GHz processor. For 36 projected visual cones and 30 million starting voxels, the average computation time was less than 5 minutes.

4. Results and discussions

The NPR 2.8 baseline jet which was used to produce the 0.9mm Mach disk for refining the code is presented in Fig. 12, while Table 1 provides the corresponding details of selected key parameters. Although over-expanded jet is not the focus of this study, the code was developed by using the Mach disk as a gauge for the required level of accuracy and resolution in the reconstruction procedure. Hence, these details are provided for the purpose of completing the

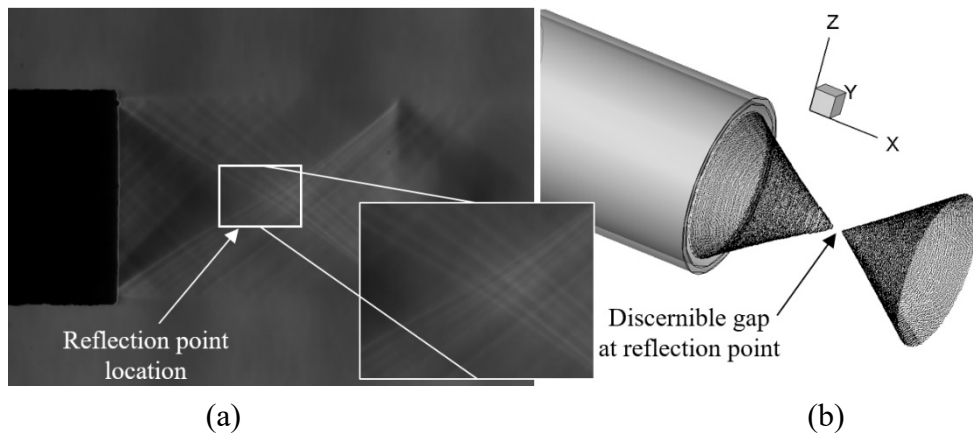


Fig. 13 Baseline nozzle's shock structures at NPR 4.0 (a) schlieren (b) reconstructed shock

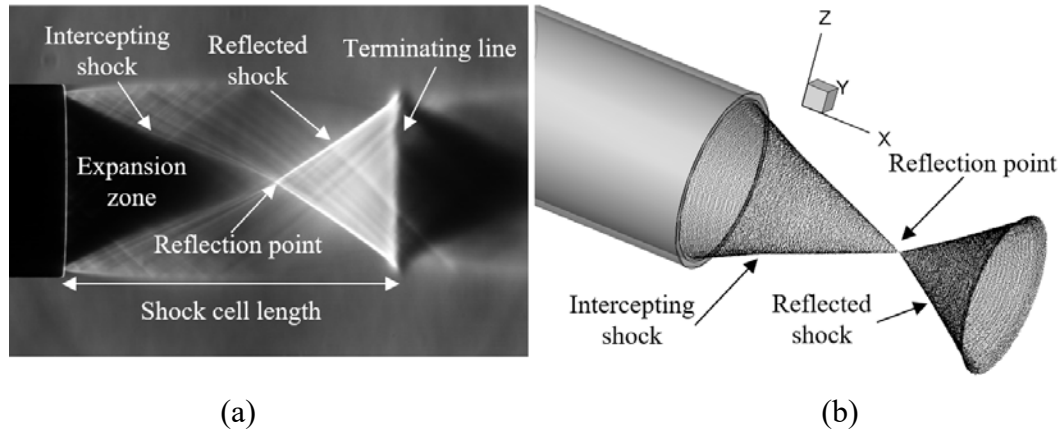
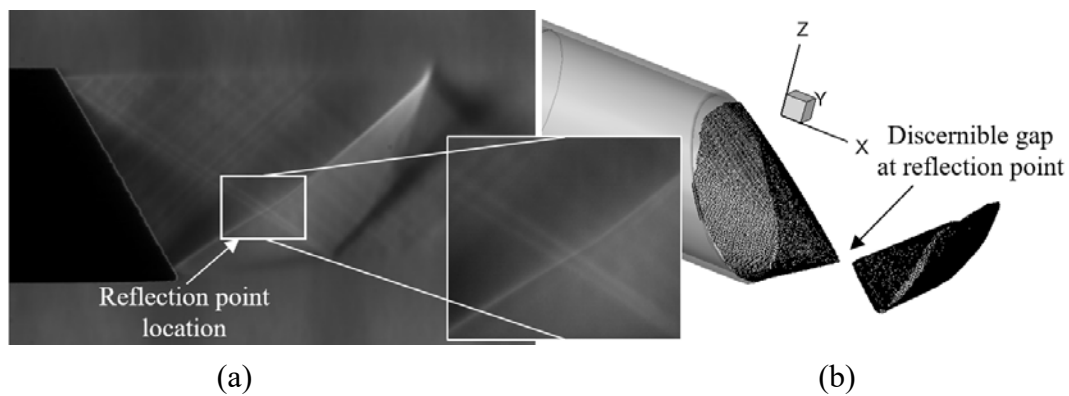


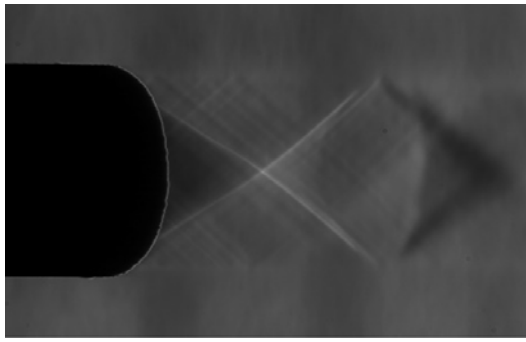
Fig. 14 Baseline nozzle's shock structures at NPR 5.0 (a) schlieren (b) reconstructed shock

study and explanation in the earlier section. Details on the procedure to obtain measurements from the schlieren images can be found in section 4.2.

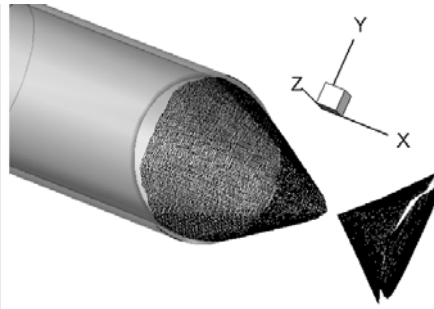
4.1 General observations

The reconstructed shock structures for the baseline jet at NPR 4.0 and 5.0 are presented in Figs. 13 and 14 while the results for the bevelled jets at NPR 4.0 and 5.0 are illustrated in Figs. 15 and 16 respectively. Beveling the nozzle shifts the reflection point towards the longer lip of the nozzle, as observed in the results for both NPR 4.0 and 5.0 in Figs. 15 and 16 respectively. Intercepting shocks are formed when compression waves coalesce, and the angle at which the intercepting shock forms is largely dependent on the initial expansion fan angles as well as the



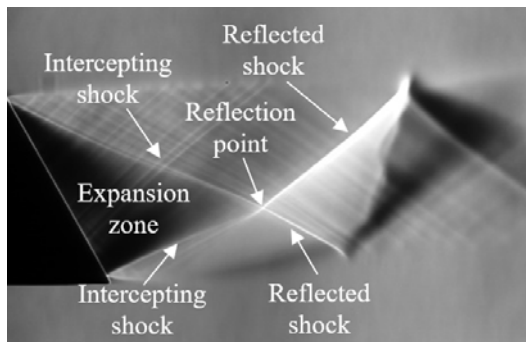


(c)

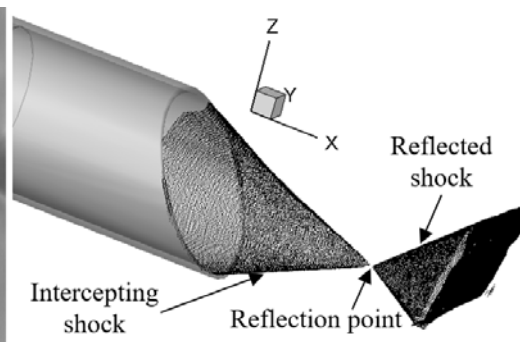


(d)

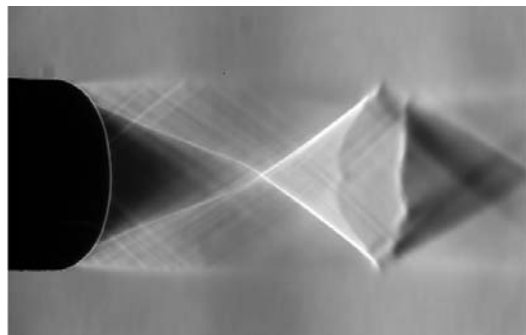
Fig. 15 Bevelled nozzle's shock structures at NPR 4.0 (a) schlieren at 0° viewpoint (b) reconstructed shock (c) schlieren at 90° viewpoint (d) reconstructed shock



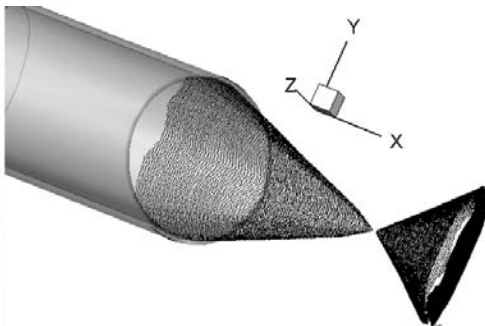
(a)



(b)



(c)



(d)

Fig. 16 Bevelled nozzle's shock structures at NPR 5.0 (a) schlieren at 0° viewpoint (b) reconstructed shock (c) schlieren at 90° viewpoint (d) reconstructed shock

constant pressure streamline. Bevelling of the nozzle and allowing the expansion fan to form earlier near the shorter lip of the nozzle appears to have altered the conditions, leading to a smaller intercepting shock angle from the shorter lip. The converse holds true for the intercepting shock from the longer lip, hence producing a nett effect of the reflection point sitting closer to the longer lip of the nozzle.

At the reflection point location, the intercepting and reflected shocks appear to be disjointed in the NPR 4.0 reconstruction results of both nozzles, as illustrated in Figs. 13(b) and 15(b). This is a non-physical observation and can be attributed to the nature of the schlieren images captured during NPR 4.0 operating conditions. The schlieren image of the NPR 4.0 baseline nozzle presented in Fig. 13(a) shows the presence of many additional edge features near the reflection point location. For the NPR 4.0 bevelled nozzle case, the schlieren image as illustrated in Fig. 15(a) shows the presence of an extra edge line emanating from the shorter nozzle lips (or 90° azimuthal angle of the nozzle exit), running parallel to the intercepting shock, and extending all the way past the reflection point location to the reflected shock. These types of edge features contribute to ambiguities and inaccuracies during the shock wave silhouette image generation process, hence resulting in a disconnection of the intercepting and reflected shocks in the final reconstructed shock structures.

In contrast, for the NPR 5.0 baseline and bevelled jets, the schlieren image in Figs. 14(a), 16(a) and 16(c) all display strong contrast and clearly defined edges, hence reconstructed results do not encounter the same issues experienced by the NPR 4.0 baseline and bevelled jets. With an increase in NPR value, the intercepting shock angle decreases, and the reflection point shifts further downstream. Density variations across shock waves become stronger, allowing the experimental setup to be optimally adjusted to obtain schlieren images with better shock wave contrast and clearer edges that are most suitable for the reconstruction.

For the same NPR value across the two nozzles, the bevelled nozzle appears to have missing shock surfaces near the shorter lip of the nozzle, as illustrated in Figs. 15 and 16. This can be attributed to the bevelled nozzle line-of-sight blockage problem and was heuristically

mitigated by linear extrapolation of shock wave edge maps as explained and illustrated in an earlier section. Striations may also be observed in the reconstructed cones and can be attributed to the nature of the space discretization techniques. To a limited extent, these effects may be reduced with the use of a higher resolution camera to create higher resolution silhouette images, along with pre-defining higher voxel resolution in the initial bounding box. However, this comes with heavier computational cost. For the current application, these options were not necessary as the prevailing resolution is sufficient and any further increment in resolution will not yield additional insights into the flow behaviour.

4.2 Quantitative evaluations

Dimensions of selected key parameters measured directly from the schlieren images and numerically from the reconstruction are illustrated for the baseline and bevelled nozzle in Tables 2 and 3 respectively. The definition of these key parameters can be found in Figs. 9(a) and 11(a). All measured angles were obtained based on measured lengths and trigonometry, though the errors of angles were not provided as there is a natural bias of large errors for angles close to zero. Schlieren image key parameters' dimensions were obtained by multiplying the key parameters' pixel dimensions with the image-to-world magnification factor, whereby the magnification factor was obtained by using the nozzle outer diameter as reference length and is independent from the magnification factor obtained from camera calibration. In the schlieren

Table 2: Reconstructed shock cone key parameters for baseline jet

	Schlieren images	Reconstructed shock cone	Percentage error
Baseline nozzle, under-expanded flow condition (NPR 4.0)			
D _{sc}	11.55 mm	11.34 mm	1.82

X_{RP}^1	9.20 mm	9.10 mm	1.09
X_{CL}	17.58 mm	17.50 mm	0.46
θ_{IS}	33.6°	33.1°	-
θ_{RS}	36.3°	36.1°	-
Baseline nozzle, under-expanded flow condition (NPR 5.0)			
D_{SC}	12.01 mm	12.15 mm	1.17
X_{RP}	14.60 mm	14.15 mm	3.08
X_{CL}	23.31 mm	23.57 mm	1.12
θ_{IS}	22.3°	22.3°	-
θ_{RS}	35.3°	35.1°	-

images, shock waves have a width of a few pixels, and directly using the schlieren images to obtain the key parameters' pixel dimensions will increase the subjectivity and random errors of the measurements. To address this issue, post-processed schlieren images in the form of edge maps were used instead of the raw schlieren images in order to obtain the key parameters' pixel dimensions. The associated random errors are placed at ± 4 pixels and is always under 2% for the lengths of key parameters under consideration.

For the reconstruction results, key parameters were numerically extracted from the reconstructed VH. The accuracy of these results was limited by practical limitations of the pre-defined voxel and image resolution, accuracy of the focal length obtained from the initial laboratory camera calibration procedure (overall mean error of 0.63 pixels), accuracy of the

36

Table 3: Reconstructed shock cone key parameters for bevelled jet²

¹ Due to the presence of a gap at the reflection point, the midpoint between the reflection points of the intercepting and reflected shocks was used to obtain X_{RP} for the reconstructed shock cone.

² Due to the asymmetry of the reconstructed shocks for the bevelled nozzle, only shock angles for the image plane illustrated in Fig. 15(a) and Fig. 16(a) are illustrated.

35

	Schlieren images	Reconstructed shock cone	Percentage error
Bevelled nozzle, under-expanded flow condition (NPR 4.0)			
X_{RP}^1	9.08 mm	9.54 mm	5.07
$\theta_{IS_90^\circ}$	33.7°	36.5°	-
$\theta_{IS_270^\circ}$	31.6°	31.6°	-
$\theta_{RS_90^\circ}$	40.4°	40.7°	-
$\theta_{RS_270^\circ}$	32.2°	38.3°	-
Bevelled nozzle, under-expanded flow condition (NPR 5.0)			
X_{RP}	14.79 mm	15.73 mm	6.36
$\theta_{IS_90^\circ}$	22.6°	22.1°	-
$\theta_{IS_270^\circ}$	23.3°	23.8°	-
$\theta_{RS_90^\circ}$	42.8°	40.9°	-
$\theta_{RS_270^\circ}$	30.4°	30.4°	-

semi-synthetic camera matrices and accuracy of the edge maps that were generated. Of these limitations, the final two points will receive additional attention in the following sub-sections.

When comparing key parameters derived from the schlieren images and the reconstruction, the average error for the reconstructions' key parameters such as, shock cone diameter (D_{SC}), reflection point location (X_{RP}) and shock cell length (X_{CL}) is about 2.5%, with the maximum error not exceeding 6.4%. For the circular jet cases, the average error was about 1.5%. The low error margin coupled with the voxel sizes of the reconstructed shock cones provided earlier suggest that the errors in the reconstructed shock cones are in the range of a few voxels, indicating any further improvement would require the use of sub-voxel accurate schemes. The bevelled jets tend to have larger errors as compared to the baseline jets, with an average error of 5.7%. This can be explained by focusing on the differences in their image processing procedures where the dominant source of error is attributed to (explained in

greater detail in a later section). For the baseline jet, only one schlieren image was required due to the axisymmetric property of the jet. In contrast, the bevelled jet required 10 schlieren images captured at different viewpoints. A larger number of schlieren images used to generate the silhouette images will inevitably mean a higher chance for the bevelled jet's image processing procedure to introduce additional errors into the silhouette images. Going by the same line of thought, the errors associated with extending this technique to fully asymmetric problems may increase even further.

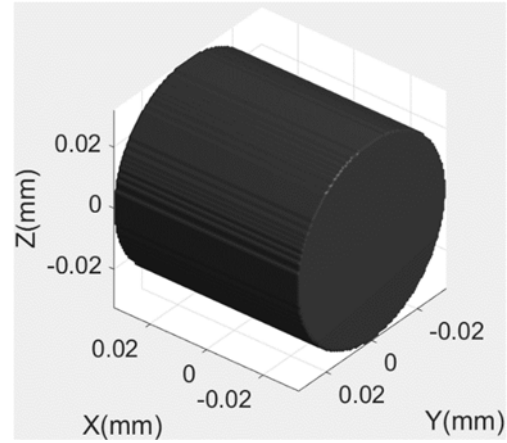
4.2.1 Semi-synthetic camera matrices

From Figs. 13(b) and 14(b), the reconstruction results can be observed to have axisymmetric geometrical properties about the jet axis, which is consistent with schlieren images of the shock structure taken from multiple view angles as mentioned earlier on. This was within expectations due to the use of the semi-synthetic camera parameters, leading to 36 cameras possessing even angular spacing of 10° and equal orthogonal distance of the focal length f relative to the jet axis (see Fig. 7(b)). The lack of ellipses or other irregular geometries in the results is a good indication that camera parameters are accurate enough to perform reconstruction at low enough errors such that it cannot be visually detected in the results.

Nevertheless, even though the reconstructed results of the baseline jets appear axisymmetric, there are still errors associated with some of the extracted parameters, as illustrated in Table 2. It will be useful to understand the origins of these errors, be it from the semi-synthetic camera parameters or the image processing procedures. A synthetic test was designed to narrow down the source of error by examining the performance of the semi-synthetic camera parameters. To

$$SYN = \begin{bmatrix} 0 & \dots & \dots & 0 \\ \vdots & \ddots & 0 & 0 & 0 \\ \vdots & 0 & 1 & 1 & 0 \\ \vdots & 0 & 1 & 1 & 0 \\ 0 & \dots & \dots & \ddots & 0 \end{bmatrix}$$

(a)



(b)

Fig. 17 Synthetic test (a) synthetic silhouette image with 2×2 cell of ones (b) reconstructed VH generated from synthetic silhouette image on the left

conduct this test, a synthetic silhouette image was generated by creating a 1024×1024 matrix of zeroes with 2×2 cell of ones at the centre of the matrix, as illustrated in Fig. 17(a). This image was then assigned to all 36 camera matrices and volume carving was conducted to obtain the visual hull. Theoretically, the real-world representation of the VH created from this image should be a cylinder with equal length and diameter. Since the criterion for a VH to be reconstructed is for sampled voxels to lie within all 36 projected visual cones, and the use of a very small silhouette generated with only 2 pixels in a single direction leads to very low aspect ratio visual cones being projected, the litmus test for the accuracy of the camera matrices will simply be to observe and see if anything can be reconstructed. In the event of a reconstruction failure, the 2×2 cell of ones will be increased to 4×4 , 6×6 and so forth until reconstruction of a VH is successful. The number of pixels of the silhouette can then be used as a quantitative indicator of the errors associated with the camera matrices.

The results for the reconstruction are illustrated in Fig. 17(b), with over 800,000 remaining voxels out of a starting of 4 million voxels. The visually boxy (striations) reconstructed VH is an indicator of resolution limitations rather than inaccuracy of the camera matrices. The

successful reconstruction along with the VH centred at the (0,0,0) location can be considered as a direct proof of the perfect alignment and accuracy of the camera matrices. To complete the study, the test was repeated with the introduction of errors into one of the camera matrix's external parameters. This created a misalignment for the camera and should result in the intersection of the projected visual cones from 35 cameras instead of all 36 cameras. Indeed, when the volume carving was conducted, no VH was reconstructed and the reconstruction fails during the projection of the visual cone from the misaligned camera. Finally, the test was repeated once again, but with errors introduced into one of the camera matrix's principal point. Again, no VH was reconstructed and the reconstruction fails at the camera with the wrong parameters. With these test results, there is sufficient evidence to conclude that the semi-synthetic camera matrices are performing as designed, and errors of the reconstructed shock structures originate solely from the image processing procedure.

4.2.2 Image processing procedures

The image processing procedures were assessed next. Since the edge detection and manual spline fitting method was used interchangeably, a comparison will be provided here. The edge maps of the baseline NPR 4.0 jet obtained from the edge detection method is illustrated in Fig. 18(a), and with the manual spline fitting method as illustrated in Fig. 18(b). The blue crosses in Fig. 18(b) mark the locations that were manually selected on the image, and it must be highlighted that they were not part of the edge map. The edge maps generated from both methods were then further processed to obtain their corresponding silhouette image, before proceeding to volume carving.

The VH results for both methods are shown in Fig. 19, with no observable difference between them. This suggests that the two methods are equally accurate for visualization purposes. The

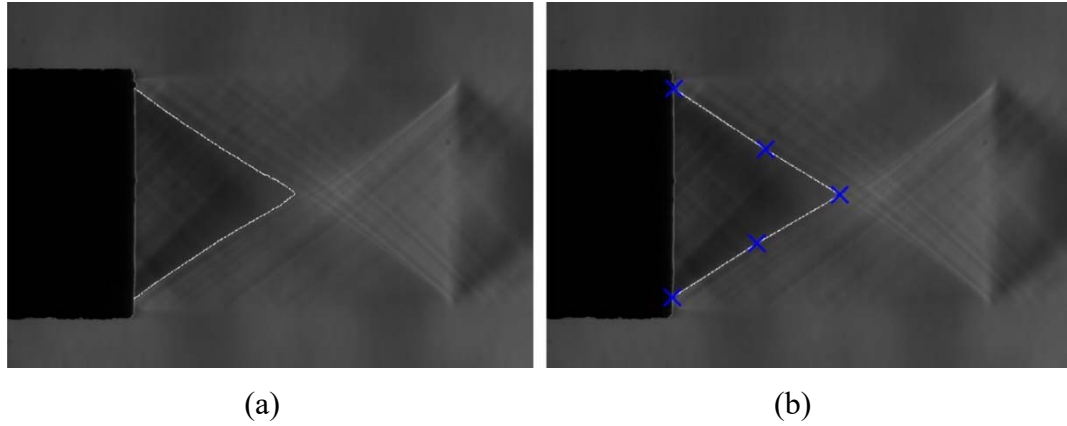


Fig. 18 Edge map obtained from (a) edge detection method (b) manual spline fitting method

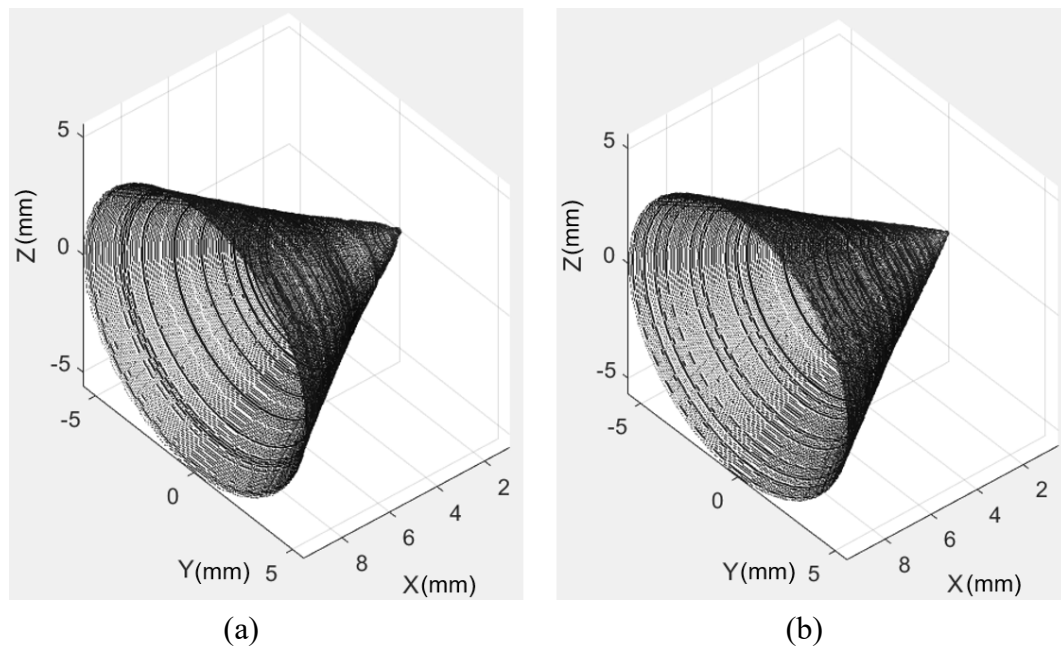


Fig. 19 Reconstruction results obtained from (a) edge detection method (b) manual spline fitting method

geometrical properties of both reconstructed shocks were extracted and given in Table 4. It can be observed that there are differences in results between the two methods, though it is not immediately obvious which method performs better. The diameter of shock cone obtained from edge detection method appears to be closer to the dimensions obtained directly from the

schlieren images, while the manual spline fitting method offers lower errors for the reflection point location. The discrepancy of the parameters is a clear indicator that the image processing procedure is a source of errors for the reconstructed VH.

Table 4: Comparison of geometrical properties for baseline nozzle at NPR 4.0

	Schlieren images	Reconstructed shock cone	Percentage error
Edge detection method			
D _{SC}	11.55 mm	11.34 mm	1.82%
X _{RP}	9.20 mm	8.70 mm	5.43%
θ_{IS}	33.6°	33.1°	-
Manual spline fitting method			
D _{SC}	11.55 mm	11.25 mm	2.60%
X _{RP}	9.20 mm	9.23 mm	0.33%
θ_{IS}	33.6°	31.1°	-

The edge detection method is a precise method that offers edge maps to be generated in a consistent and efficient manner under ideal conditions, or when the input images have a high SNR. If the input images have a low SNR, the edge detection method will not be robust and can no longer be considered efficient as images from multiple views cannot be processed with the same set of parameters anymore. Finding the set of optimal parameters which includes the edge threshold, standard deviation for the gaussian filter and area opening threshold all requires experience and judgement that cannot be replaced by algorithms easily. A possible direction to automate the process can be to integrate machine learning concepts and train these parameters with huge datasets but that is beyond the scope of this study. Hence, for images that have low SNR, generation of the edge map using the edge detection method becomes a time-consuming and inefficient process.

In contrast, while the manual spline fitting method appears to be cumbersome and not as systematic, they do hold certain advantages over the edge detection method. For input images that are not ideal for edge detection algorithms, the manual spline fitting method could be more robust and allows the user to incorporate posteriori knowledge directly in the post-processing of the schlieren image. This is advantageous as the human perception is still widely conceived as the most efficient and powerful image processor [38, 39] even after decades of computer vision research. The manual spline fitting method will also be robust for a vastly different study, such as in supersonic impinging jet applications, while the same cannot be said for the edge detection method which was specially developed for the current application. Furthermore, little time is required to pick out selected points lying along a shock wave in an image. While manual spline fitting method leads to a certain degree of subjectivity associated with the selection of the points to fit the splines, this can be minimized with careful selection of the shock wave points, and the random error associated with this subjectivity is estimated to be at ± 4 pixels within the present study.

5. Conclusions

A novel approach for 3D shock structure reconstruction was proposed, based on schlieren images and a shape-from-silhouette image-processing technique known as voxel-based visual hull. Due to the very small dimensions of certain shock structures with relatively large projection distances, precise camera parameters were found to be crucial in obtaining accurate reconstructed shocks. This provided the motivation behind the present approach of integrating a conventional camera calibration process with synthetically generated camera parameters. By making use of the experimentally calibrated focal length during the synthetic camera parameters generation process, useful geometrical information can be numerically extracted from the reconstructed shock structures.

Shock structures for baseline and bevelled jets were reconstructed under the assumptions of no geometrical concavities and steady shock systems, with extracted key parameters of the reconstructed baseline and bevelled jet having an average error of 2.5%. Extending the technique to more complicated flow scenario such as the bevelled jet brings about an additional challenge due to the schlieren line-of-sight blockage from the nozzle. This was overcome with a heuristic linear extrapolation of the shock wave edge maps during the silhouette image generation process. The accuracy of the technique is strongly dependent on the quality of the schlieren images, with high shock wave contrast and clearly defined edges offering the best reconstruction results. The presence of multiple weak shocks decreases the SNR of the acquired images while strong shocks have the most potential in generating schlieren images of shock waves with high image contrast when the schlieren system is appropriately over-ranged.

The performance of the semi-synthetic camera parameters and the image processing procedures were evaluated, and error sources were identified to be solely originating from the image processing procedures. By directly reconstructing the shock waves without the need to first obtain the global velocity or density field, this provides the advantage of low hardware requirements, low computation time, and high-resolution reconstructed shock waves. The proposed technique is particularly well suited for steady compressible flow scenarios with optical access to conduct schlieren experiments, with the presence of strong shocks to obtain optimal schlieren images for best reconstruction results. The success of the present unique approach highlights the potential of its application towards more complex 3D shock reconstructions in future studies, particularly in strong shocks application whereby existing 3D experimental techniques are not particularly well suited for. Examples of potential

application includes optimization of multi-shock designs at supersonic inlet, study of shock geometries in hypersonic flows and formation of shock systems in supersonic impinging jets.

Acknowledgment

The authors gratefully acknowledge support for the study through a Singapore Ministry of Education AcRF Tier-2 grant (Grant number: MOE2014-T2-1-002), as well as support for the first author through a NTU Nanyang President Graduate Scholarship, and facility support from Temasek Laboratories at National University of Singapore. Valuable scientific discussions with Q. Wang of Shanghai Jiao Tong University are also gratefully acknowledged.

References

1. Franquet, E., Perrier, V., Gibout, S., and Bruel, P., *Free underexpanded jets in a quiescent medium: a review*. Progress in Aerospace Sciences, 2015. **77**: p. 25-53.
2. Panda, J., *Shock oscillation in underexpanded screeching jets*. Journal of Fluid Mechanics, 1998. **363**: p. 173-198.
3. Mitchell, D.M., Honnery, D.R., and Soria, J., *The visualization of the acoustic feedback loop in impinging underexpanded supersonic jet flows using ultra-high frame rate schlieren*. Journal of Visualization, 2012. **15**(4): p. 333-341.
4. Wernet, M.P., *Application of tomo-PIV in a large-scale supersonic jet flow facility*. Experiments in Fluids, 2016. **57**(9): p. 144.
5. Venkatakrishnan, L., *Density measurements in an axisymmetric underexpanded jet by background-oriented schlieren technique*. AIAA Journal, 2005. **43**(7): p. 1574.

6. Papamoschou, D., *A two-spark schlieren system for very-high velocity measurement*. *Experiments in Fluids*, 1989. **7**(5): p. 354-356.
7. Papamoschou, D., *Structure of the compressible turbulent shear layer*. *AIAA Journal*, 1991. **29**(5): p. 680-681.
8. Papamoschou, D., *Mach wave elimination in supersonic jets*. *AIAA Journal*, 1997. **35**(10): p. 1604-1611.
9. Papamoschou, D. and Bunyajitradulya, A., *Evolution of large eddies in compressible shear layers*. *Physics of Fluids*, 1997. **9**(3): p. 756-765.
10. Papamoschou, D. and Roshko, A., *The compressible turbulent shear layer: an experimental study*. *Journal of Fluid Mechanics*, 1988. **197**: p. 453-477.
11. New, T.H. and Tsai, H.M., *Experimental investigations on indeterminate-origin V-and A-notched jets*. *AIAA Journal*, 2007. **45**(4): p. 828-839.
12. New, T.H. and Tsovolos, D., *Influence of nozzle sharpness on the flow fields of V-notched nozzle jets*. *Physics of Fluids*, 2009. **21**(8): p. 084107.
13. New, T.H. and Tsovolos, D., *On the vortical structures and behaviour of inclined elliptic jets*. *European Journal of Mechanics-B/Fluids*, 2011. **30**(4): p. 437-450.
14. Gutmark, E., Schadow, K., and Yu, K., *Mixing enhancement in supersonic free shear flows*. *Annual Review of Fluid Mechanics*, 1995. **27**(1): p. 375-417.
15. Wu, J. and New, T.H., *An investigation on supersonic bevelled nozzle jets*. *Aerospace Science and Technology*, 2017. **63**: p. 278-293.
16. Wlezien, R. and Kibens, V., *Influence of nozzle asymmetry on supersonic jets*. *AIAA Journal*, 1988. **26**(1): p. 27-33.
17. Settles, G.S. and Hargather, M.J., *A review of recent developments in schlieren and shadowgraph techniques*. *Measurement Science and Technology*, 2017. **28**(4): p. 042001.

18. Atcheson, B., Heidrich, W., and Ihrke, I., *An evaluation of optical flow algorithms for background oriented schlieren imaging*. *Experiments in Fluids*, 2009. **46**(3): p. 467-476.
19. Raffel, M., *Background-oriented schlieren (BOS) techniques*. *Experiments in Fluids*, 2015. **56**(3): p. 1-17.
20. Hayasaka, K., Tagawa, Y., Liu, T., and Kameda, M., *Optical-flow-based background-oriented schlieren technique for measuring a laser-induced underwater shock wave*. *Experiments in Fluids*, 2016. **57**(12): p. 179.
21. Hargather, M.J., Lawson, M.J., Settles, G.S., and Weinstein, L.M., *Seedless velocimetry measurements by schlieren image velocimetry*. *AIAA Journal*, 2011. **49**(3): p. 611-620.
22. Venkatakrishnan, L. and Meier, G., *Density measurements using the background oriented schlieren technique*. *Experiments in Fluids*, 2004. **37**(2): p. 237-247.
23. Sourgen, F., Leopold, F., and Klatt, D., *Reconstruction of the density field using the colored background oriented schlieren technique (CBOS)*. *Optics and Lasers in Engineering*, 2012. **50**(1): p. 29-38.
24. Atcheson, B., Ihrke, I., Heidrich, W., Tevs, A., Bradley, D., Magnor, M., and Seidel, H.-P. *Time-resolved 3d capture of non-stationary gas flows*. in *ACM Transactions on Graphics (TOG)*. 2008. ACM.
25. Nicolas, F., Todoroff, V., Plyer, A., Le Besnerais, G., Donjat, D., Micheli, F., Champagnat, F., Cornic, P., and Le Sant, Y., *A direct approach for instantaneous 3D density field reconstruction from background-oriented schlieren (BOS) measurements*. *Experiments in Fluids*, 2016. **57**(1): p. 13.
26. Le Sant, Y., Todoroff, V., Bernard-Brunel, A., Le Besnerais, G., Micheli, F., and Donjat, D. *Multi-camera calibration for 3DBOS*. in *17th International Symposium on Applications of Laser Techniques to Fluid Mechanics*. 2014.

27. Furukawa, Y. and Ponce, J., *Accurate camera calibration from multi-view stereo and bundle adjustment*. International Journal of Computer Vision, 2009. **84**(3): p. 257-268.
28. Torr, P.H. and Zisserman, A. *Feature based methods for structure and motion estimation*. in *Workshop on Vision Algorithms*. 1999. Springer.
29. Slabaugh, G., Schafer, R., Malzbender, T., and Culbertson, B. *A survey of methods for volumetric scene reconstruction from photographs*. in *Volume Graphics 2001*. 2001. Springer.
30. Dyer, C.R., *Volumetric scene reconstruction from multiple views*, in *Foundations of Image Understanding*. 2001, Springer. p. 469-489.
31. Lowe, D.G., *Distinctive image features from scale-invariant keypoints*. International Journal of Computer Vision, 2004. **60**(2): p. 91-110.
32. Bay, H., Ess, A., Tuytelaars, T., and Van Gool, L., *Speeded-up robust features (SURF)*. Computer Vision and Image Understanding, 2008. **110**(3): p. 346-359.
33. Baumgart, B.G., *Geometric modeling for computer vision*. 1974, DTIC Document.
34. Laurentini, A., *The visual hull concept for silhouette-based image understanding*. IEEE Transactions on Pattern Analysis and Machine Intelligence, 1994. **16**(2): p. 150-162.
35. Matusik, W., Buehler, C., Raskar, R., Gortler, S.J., and McMillan, L. *Image-based visual hulls*. in *Proceedings of the 27th Annual Conference on Computer Graphics and Interactive Techniques*. 2000. ACM Press/Addison-Wesley Publishing Co.
36. Zhang, Z., *A flexible new technique for camera calibration*. IEEE Transactions on Pattern Analysis and Machine Intelligence, 2000. **22**(11): p. 1330-1334.
37. Tordoff, B., *Carving a dinosaur*. 2016, MATLAB Central File Exchange.
38. Fleuret, F., Li, T., Dubout, C., Wampller, E.K., Yantis, S., and Geman, D., *Comparing machines and humans on a visual categorization test*. Proceedings of the National Academy of Sciences, 2011. **108**(43): p. 17621.

Lim H.D., New T.H., Mariani R. and Cui Y.D. (2018) Visual-hull based 3D reconstruction of shocks in under-expanded supersonic bevelled jets. Experimental Thermal and Fluid Science, Vol. 99, pp. 458-473

39. Thorpe, S.J., *Image processing by the human visual system*, in *Eurographic Seminars (Tutorials and Perspectives in Computer Graphics)*. 1991, Springer Berlin Heidelberg: Berlin, Heidelberg. p. 309-341.